1   **Revision 2**

2

3   **Mudrock micro-fabric explored through charge contrast imaging**

4

5   Buckman, Jim[a], Mahoney, Carol[b], März, Christian[c], Wagner, Thomas[d], & Blanco,

6   Vladimir[e]

7

8   [a]*Institute of Petroleum Engineering, Heriot-Watt University, Riccarton, Edinburgh,*

9   *EH14 4AS, Scotland.*

10

11   [b]*School of Civil Engineering and Geosciences, Cassie Building, Newcastle University,*

12   *Newcastle upon Tyne, NE1 7RU, United Kingdom.*

13

14   [c]*School of Earth and Environment, University of Leeds, LS2 9JT, United Kingdom.*

15

16   [d]*The Lyell Centre, Heriot-Watt University, Riccarton, Edinburgh, EH14 4AS, Scotland.*

17

18   [e]*Instituto Colombiano del Petróleo, Ecopetrol, Bucaramanga, Colombia.*

19

20   **Abstract:** Visual inspection (optical microscope point counting) and silica abundance

21   show that laminated shale from the Late Cretaceous of Colombia contains high levels of

22   detrital quartz silt and sand particles. Closer examination using the charge contrast

23   imaging (CCI) technique, however, illustrates that much of the quartz is authigenic

24   micro-quartz, and thus not exclusively of detrital origin. In addition, many 'sand' grains

25   that otherwise appear to represent simple detrital quartz particles are actually of biogenic

26   origin, representing the tests of agglutinated foraminifera, formed from cemented silt-

27   sized quartz particles. Finally, CCI shows that original detrital grains have undergone

28   authigenic modification, with both syntaxial overgrowths and micro-quartz. Without

29   recognition of these features, the relative proportion of detrital quartz (sand) would

30   otherwise be greatly overestimated, with important implications for environmental

31   interpretation. Furthermore, the recognition of biogenic structures, including agglutinated

32   foraminifera, provides additional environmental information that otherwise could be

33   easily overlooked.

34   **Keywords:** Shale, silt, quartz cementation

35

Introduction

36

37   Mudrocks represent approximately 65% of the stratigraphic record on continents

38   (Ibbeken & Schleyer, 1991) and are a significant proportion of marine sediments (Blatt,

39   1970; Ibbeken & Schleyer, 1991). They are economically significant, representing

40   sources and seals for hydrocarbon resources (Al-Bazali et al., 2005; Olabode et al., 2012)

41   as well as potential seals for carbon dioxide storage / carbon sequestration (Olabode et

42   al., 2012) and can contain metal enrichments up to low grade ore levels (Anjum et al.,

43   2012). Although superficially simple and supposedly homogenous, mudrocks are highly

44   variable at the micro-scale in terms of composition and texture (see examples in Camp et

45   al., 2013; Milliken 2014; Milliken et al., 2016) documenting the complex overlying /

46   integrated effects of dynamic primary depositional conditions and post-depositional

47   diagenetic alteration. Comprising a wide range of dominantly clay-size clay minerals

48   (smectite, illite, kaolinite), they also feature varying contents of silt and sand particles

49   (quartz, feldspars and micas), organic matter (charcoal, kerogen, bitumen, phytoclasts),

50   and siliceous and calcareous micro-skeletal materials (diatoms, radiolaria, foraminifera,

51   etc). Fabric can range from massive to fissile (mudstone versus shale), and at the

52   microscopic level, porosity / permeability, clay mineral composition and orientation can

53   be drastically altered through diagenesis during burial, including the formation of

54   authigenic phases such as calcite, quartz, pyrite, marcasite and iron-oxides. Mudrocks

55   therefore provide a significant repository of information regarding the depositional

56   environment and subsequent diagenetic changes through time, with their study becoming

57   an increasing focus of research (Bennett et al., 1991; Camp et al., 2013; Lazar et al.,

58   2015).

3

59   The present study illustrates detailed results from charge contrast imaging (CCI)

60   performed on a Cretaceous marine shale that has undergone substantial modification

61   through massive authigenic quartz induration. The content of quartz 'sand', defined as

62   quartz grains of 63 micrometer to 2 millimeter in diameter, in the shale had previously

63   been estimated based on Si content from XRF, XRD of the >2μm fraction and optical

64   microscope point counting of sand-sized grains in thin-section. Examination by scanning

65   electron microscopy (SEM) illustrates that much of the original depositional information

66   has been masked by pervasive silicification of the shale, a feature that is not obvious from

67   examination of hand specimens, thin-sections or element abundance patterns, therefore

68   leading to gross over-estimation of the original sand fraction.

69   We tested a low-vacuum SEM technique of charge contrast imaging (CCI) to elucidate

70   valuable information concerning the original depositional conditions of this shale. CCI

71   has previously been shown to have applications on a range of other geological materials,

72   where it has been utilized to illustrate crystal zoning, authigenic overgrowths, cement

73   fabrics and healed fractures (Watt et al., 2000; Doehne and Carson, 2001; Cuthbert and

74   Buckman, 2005; Buckman et al., 2016). The technique is comparable to

75   Cathodoluminescence within the SEM (Griffin 1997; Griffin 2000; Buckman et al.,

76   2016), with contrast being controlled by differences in surface conductivity through

77   subtle variations in composition and structural defects, affecting electron emission

78   (Buckman et al., 2016). As shown in this study, CCI provides highly valuable

79   information that improves the interpretation of silt bearing mudrocks which have

80   undergone heavy quartz cement precipitation (see Milliken, 2013; Milliken et al., 2016),

81   akin to applications on carbonate rocks (Buckman et al., 2016).

82   In addition, selected XRF and XRD data were collected to help interpretation of possible

83   mechanisms for the observed occurrence of silicification.

84

85   **Materials and Methods**

86   The main sample examined (Z39) is a Late Cretaceous shale from the Coniacian of the

87   Chipaque Formation from the Valle Medio del Magdalena (MMV) province, Colombia.

88   The shale was collected from a surface outcrop at a road cutting in the Serranía de las

89   Quinchas region (Fig. 1). An additional eight samples of 'shale' from the MMV and

90   Eastern Cordillera (EC), from a range of stratigraphic horizons, related to Z39, and

91   known burial depths, within the Cretaceous sequence (Fig. 2) were also examined and

92   compared to the main sample. All samples were trimmed and impregnated with resin,

93   then prepared as polished thin-sections, for examination by scanning electron microscopy

94   (SEM). A Quanta 650 field-emission SEM was used, operated in low-vacuum mode,

95   utilizing a large-field gaseous secondary electron detector (LF-GSED). Essentially, the

96   charge contrast imaging (CCI) technique was used, following the method outlined in

97   Buckman et al. (2016), which provides information similar to those achieved through

98   cathodoluminescence (such as details of quartz overgrowths), by utilizing differences in

99   surface charge build up, which effects image contrast and brightness. Thin-sections were

100   examined uncoated, and images were collected at 20kV, with a spot size of 4.5, a detector

101   bias of around 50% and a scan rate of between 5 and 20 μs. The standard quad

102   backscattered electron (BSE) detector, and a Gatan mini-cathodoluminescence (CL)

103   detector were utilized with similar imaging parameters to that of the LF-GSED, with the

104   addition that for CL a scan rate of between 800 μs and 2.5 ms were used. In addition, an

5

105   Oxford Instruments X-Max^N 150 energy dispersive x-ray (EDX) detector was used for

106   elemental mapping, under the same operating conditions as for BSE imaging, with

107   between 20 and 30 full frame scans per map.

108   A Seimens model D500 XRD was used to analyse powdered samples, for both the greater

109   than 2 µm and the less than 2 µm fraction (35 samples). The less than 2 µm fraction were

110   analysed without treatment, with ethylene glycol (to differentiate expandable clays), and

111   thermally to differentiate kaolinite and chlorite. Samples were analysed from all

112   locations where thin-sections have been examined, with the exception of La Cristalina

113   and La Marina. Where possible, this included a sample from the same bed as the thin-

114   sections. Additionally, a single crushed whole rock sample of Z39 was analysed using a

115   Bruker D8 Advance powder diffractometer.

116   Samples from each location (184 samples) were also frozen, freeze-dried and ground in

117   an agate ball mill for subsequent chemical analysis by XRF (Philips PW 2400). Around

118   600 mg of each sample were mixed with 3600 mg of a 1 + 1 di-lithium tetraborate +

119   lithium metaborate ($Li_2B_4O_7$ + $LiBO_2$) mixture, pre-oxidized at 500˚C with NH_4NO_3, and

120   fused to homogeneous glass beads. Glass beads were analyzed for major and minor

121   elements. Analytical precision and accuracy were better than 5%, as checked by in-house

122   and international standard materials. Data were then used to calculate values for Zn/Al,

123   Cu/Al and Ni/Al, and an element enrichment factor (EEF) for Mo, V, U and Zn relative

124   to average shale (see Wedepohl, 1971).

125

126   **Results**

6

127   Analyses of backscattered (BSE) images of the thin-section (Z39) indicate that much of

128   the shale is composed of quartz, with minor fine-sand particles, silt-size particles

129   (typically up to 10 μm), a background of micro-quartz (sub-micrometer to micrometer-

130   size), and illite clay (Fig. 3). In addition, high porosity is suggested, which is typically

131   spherical to lenticular in morphology and excessively large (Fig. 3), indicating that much

132   of this porosity is likely an artifact of grain plucking during sample preparation rather

133   than a primary property of the shale.

134   Charge contrast images (CCI) taken using the LF-GSED confirm that the detrital grains

135   are generally smaller than apparent from BSE imaging, having relatively thick syntaxial

136   quartz overgrowths, and in many cases also incorporating authigenic micro-quartz (Fig.

137   4b-f). Some of the silt-size quartz particles display signs of healed cracks and fragmented

138   grains that have been re-cemented (Fig. 4c). The micro-quartz that forms the bulk of the

139   matrix has a distinctive mottled appearance when viewed by CCI, clearly differing from

140   that of detrital quartz cores or associated syntaxial overgrowths (Figs. 4b-f, 5e). This

141   authigenic micro-quartz is granular in appearance and typically around 1 μm or less in

142   size (Fig. 5e). Subtle differentiation within the micro-quartz suggests multi-phased

143   crystal growth with euhedral shaped overgrowths (Fig. 5e). In addition, some of the

144   apparent larger 'silt' particles are in fact the compressed remains of agglutinated

145   foraminifera (Fig. 5a-d). These remains are up to 100 μm in length, and typically around

146   40 μm in thickness, and vary in shape from lenticular to spherical or sub-spherical.

147   Unlike BSE or GSE images, CL-imaging proved of limited use with interpretation of the

148   current material, producing low contrast images providing no additional information (Fig.

149   6). However, EDX mapping confirmed the pervasive nature of silicification (Fig. 6d).

7

150   Other thin-sections examined, from similar mudrocks within the Middle Magdelana

151   Valley (MMV) and adjacent Eastern Cordillera (EC), may also display a moderate to

152   high degree of silicification (sample LC224 and PE119), with the occurrence of both

153   large quartz overgrowths and common granular authigenic micro-quartz that are in the

154   order of a micrometer or less in size (Fig. 7a, b). Other samples, such as C29, have only

155   a low degree of silicification, with minor granular micro-quartz within the shale matrix

156   (Fig. 7c) and no obvious quartz overgrowths. The majority of other samples examined

157   exhibit limited silicification, with only isolated detrital quartz silt particles present (Fig.

158   7d-g). An exception to this is, however, sample A240, with localized areas of micro-

159   quartz that have a more wavy morphology rather than the previously noted granular

160   texture (Fig. 7h).

161   XRD results for the greater than 2 μm coarser fraction, shows highest values recorded for

162   clay and sand, with minimal values for other phases (Table 1). Particularly high levels of

163   'sand' are found from the Pescana and Zipa localities, including sample Z39. The high

164   occurrence of quartz 'sand' is also indicated by the additional whole rock analysis of Z39,

165   which is dominated by peaks for quartz, with minor illite (Fig. 8).

166   In general, XRD analysis of the less than 2 μm fraction, shows that illite-smectite is

167   almost solely limited to Crucero, illite is found throughout, with the highest values from

168   Quemado and Algodones, and some high records from Zipa (Table 1). Kaolinite is

169   common within Pescana, Crucero and Pedregal, but low within the other analysed areas,

170   while chlorite only occurs in very small levels within the Quemado and Algodones

171   material (Table 1). For micro-quartz, most areas are low with under 10%, with higher

172   values occurring from Pescana and Zipa (Table 1).

8

173   XRF results for the ratio of Zn/Al, Cu/Al and Ni/Al are presented for all sample locations

174   (Table 2). These show relatively high enrichment in all three for sample Z39 and LC224,

175   with some enrichment for Zn/Al in PE119 (including average values across each

176   locality). The enrichment in Zn/Al is particularly notable for sample Z39 and even more

177   so in LC224 (markedly so for the average value from La Cristalina). Results for the

178   element enrichment factor (EEF) display marked enrichment in Mo, V, U and Zn for the

179   Zipa and La Cristalina sections, and Mo is also relatively enriched in La Marina,

180   Quemado and the Algodones localities (Table 3).

181

182   **Discussion**

183   The use of CCI to identify features within quartz, including silt-sized particles, has

184   previously been documented (Milliken et al., 2007; Lehmann et al., 2009; Schieber,

185   2009). These CC images closely relate to images obtained through cathodoluminescence

186   (Milliken et al., 2007; Lehmann et al., 2009; Milliken, 2013; Milliken et al., 2016), as is

187   also the case for other geological materials (Watt et al., 2000; Buckman et al., 2016).

188   CCI in comparison to SEM based CL, has the advantages of being faster and offering

189   greater resolution (Buckman et al., 2016). Despite the use of high kV and long scan

190   times, SEM-CL images (herein) of the silt particles, micro-quartz and siliceous biogenic

191   structures do not shed much light on the internal structure of the grains, with the CL

192   response being particularly weak (Fig. 6).

193   Both CL and CC imaging have been used for quartz to show evidence of *in situ* fracturing

194   and re-cementation / healing (Watt et al., 2000), which also appears to be the case for

195   some of the silt particles observed in the Colombian shale. The sparsity of such features

9

196   in our samples may be a consequence of the low number of genuine silt particles (<5%),

197   presenting limited opportunity for quartz grain-to-grain contact, as would be the case in

198   sandstone.

199   CC images of micro-quartz illustrate a mottled fabric for this sub-micrometer sized

200   material. To our knowledge, this is the first time that such a feature has been presented,

201   and confirms the variability of such material recently noted using CL in fine grained

202   shale (see Milliken et al., 2016, fig. 13b). The micro-quartz has a morphology that is

203   clearly distinct from both detrital quartz and associated syntaxial-quartz overgrowths.

204   Micro-quartz is differentiated by CCI, being typically granular in appearance (Fig. 3e, 4b,

205   5e), generally 1 µm or less in size, having a mottled appearance (Fig. 5e), and

206   occasionally with euhedral quartz overgrowths (Fig. 5e). Different from that, authigenic

207   syntaxial overgrowths on detrital quartz grains form simple euhedral forms (Fig 4b, e),

208   are often thick and occasionally exhibiting growth zonation. The latter can pass into rims

209   of amalgamated micro-quartz (Fig. 4b, e, f), which can greatly thicken the apparent size

210   of detrital grains. This distinction based on CCI is important as it provides a means of

211   differentiating detrital from authigenic quartz. Incorrect recognition of the micro-quartz

212   component could lead to overestimation of the detrital quartz (sand) input (see Table 1),

213   with important connotations for the interpretation of energy-levels during sedimentation

214   and consequently of the depositional environment (e.g., pelagic versus turbiditic and / or

215   contouritic deposition).

216

217   **Origins of silification**

218   Quartz cements are a common feature of sedimentary basins with a range of sources,

219   including 1) metastable biogenic quartz, 2) dissolution of quartz grains by pressure

220   solution and 3) the release of silica through mineral reactions (Bjørlykke and Egeberg,

221   1993), such as through the smectite-illite transformation (Elliott and Matisoff, 1996;

222   Thyberg et al., 2010) and the alteration of volcanic glass and ash (Ghiara and Petti, 1995;

223   Rani et al., 2012). For the Colombian samples (Z39, LC224, which are most heavily

224   silicified), dissolution of quartz grains through pressure solution is unlikely to supply a

225   major component, as the low levels of silt or sand sized quartz particles provide very

226   limited opportunity for grain-to-grain contacts. However, presence of authigenic silica

227   from mineral interactions or from the remobilization of biogenic silica are both possible.

228   The degree of overburden and maximum recorded temperatures of the studied materials

229   (Table 4), combined with vitrinite reflectance values and a palaeothermal gradient of 20 –

230   25˚C (Parra et al., 2009), would be consistent with the transition of smectite to mixed

231   layer illite-smectite. Examination of an XRD trace for Z39, however, shows that there is

232   no evidence of smectite or mixed layer smectite-illite (Fig. 8), or from the Zipa section

233   (Table 1), although the very presence of illite indicates that the transformation cannot be

234   totally excluded. If clay transformation was responsible for the release of silica, it would

235   have occurred after relatively high levels of compaction (see Table 4 for degree of

236   overburden), which is inconsistent with the presence of abundant 'granular' micrometer

237   sized micro-quartz. Furthermore, if clay transformation were to explain the occurrence of

238   micro-quartz within the Chipaque Formation, then the degree of silicification might be

239   expected to increase with depth (with higher temperature), which is not the case for the

240   current associations (Table 4, Fig. 7). We recognize, however, that some minor

11

241   silicification deeper within the sequence from the Eastern Cordillera may have an origin

242   from clay mineral transition, leading to a more irregular and often compressed

243   morphology (Fig. 7h), although the degree of silicification is here lower (Table 4). The

244   latter would certainly have passed through the temperature window necessary for the

245   transformation of smectite to illite, with associated release of silica, as indicated by the

246   occurrence of chlorite (Table 1), which within shales can form at temperatures of over

247   122˚C (Hurst, 1985). Volcanic activity, producing thin ash deposits, has been noted from

248   the La Luna Formation, Magdelana Valley (Galvis-Portilla et al., 2014). The latter is

249   stratigraphically equivalent to the Chipaque Formation (Guerrero, 2002), with in excess

250   of 78 ash beds recorded in a 3 to 4 metre section at the Cenomanian-Turonian boundary

251   (Erlich et al., 2003). Also, bentonite beds are present at the Cenomanian-Turonian

252   boundary within the Chipaque Formation within the Eastern Cordillera (Villamil and

253   Arango, 1994). However, Vergara (1997) has indicated that volcanic activity where

254   present in Colombia, although likely to increase marine productivity, was unlikely to be a

255   direct source of silicification. Dissolution of volcanic ash deposits and glass are unlikely

256   to contribute significantly to the observed micro-quartz production, as no direct evidence

257   of volcanic deposits have been recorded interbedded within the current heavily silicified

258   locations (Zipa and La Cristalina).

259   Another potential source of silica for the formation of micro-quartz could have been

260   metastable biogenic opal, from sponge spicules, diatom frustules or radiolaria. While no

261   direct physical evidence of biogenic opal was observed in our study samples, pyritized

262   sponge spicules have been noted from other horizons within the basin (from Pescana

263   within P145 and La Cristalina in LC224, Fig. 9), supporting a release mechanism from

12

264   biogenic silica. Geochemical support for the original deposition of biogenic opal comes

265   from a significant enrichment of trace elements (Cu, Ni, and Zn, see Table 2), all of

266   which are typical for upwelling settings, such as modern Namibia and Peru (Brumsack,

267   2006). In such upwelling settings, high primary productivity mainly by diatoms leads to

268   elevated export of large amounts of biogenic opal and organic matter enriched in trace

269   metals to the seafloor, where they get partly buried under typically reducing conditions.

270   Enrichment in Zn, Cu and Ni from the Chipaque Formation (at Zipa, including Z39), and

271   underlying Fomeque Formation (at La Cristalina, including LC224) from the MMV

272   (Table 2), and of Zn within the Chipaque Formation (at Pescana, including PE119) from

273   the EC (Table 2), strongly suggests that silicification within these horizons (with high to

274   moderate silicification) was primarily due to dissolution and migration of biogenic silica,

275   originally produced through high marine productivity. This conclusion is further

276   supported by the occurrence of a thick fractured chert horizon (from the Lidita

277   Formation) that directly overlies the Chipaque Formation (Garcia-Gonzalez, 2010). This

278   has been interpreted as representing regional high productivity linked to vigorous

279   upwelling (Villamil et al., 1999). Chert formation has been frequently documented from

280   the Cenomanian to Santonian across the northern part of South America, including the

281   EC and MMV (Tribovillard et al., 1991 ; Perez-Infante, 1996; Arango and Hay, 1999),

282   often linked with upwelling processes (Macellari and DeVries, 1987). Palaeogeographic

283   reconstructions for the wider area (Fig. 10) support regional upwelling, driven by

284   prevailing trade winds from the north-east (Erlich et al., 2003), further supporting an

285   origin for silicification from remobilization of biogenic silica.

286

13

Significance of benthic foraminifera

287

288   Agglutinated foraminifera tests, composed of detrital quartz and feldspar particles, have

289   recently been illustrated for 'cherty stringers' in Carboniferous and Devonian black

290   shales (Milliken et al., 2007; Schieber, 2009). Such foraminifera have also been

291   previously recorded from Cretaceous deep-sea black shales (e.g. Mello, 1971), including

292   benthic agglutinated and pelagic foraminifera from the Chipaque Formation (Vergara et

293   al., 1997). The recognition, through CCI, of agglutinated foraminifera, shallow infaunal

294   foragers and suspension feeders that strictly require oxygen (Kaminski & Schroder,

295   1987), implies that bottom waters or near-surface sediments were at least episodically

296   dysaerobic during deposition, if not fully aerobic. Repetitive alternations between fully

297   aerobic and slightly oxygen-depleted conditions are indeed suggested from the general

298   lack of pyrite and other sulphide phases (Table 1). This SEM-based redox interpretation

299   clearly contrasts with the overall enrichment of redox-sensitive / sulphide-forming trace

300   elements (Mo, V, U, Zn) measured in the same sample, a pattern which is commonly

301   related to anoxic or even sulfidic bottom and pore water conditions (Brumsack, 2006).

302   Such discrepancies between geochemistry- and micropaleontology-based redox

303   interpretations are not unusual and may actually be expected. It has been shown that some

304   benthic agglutinated foraminifera are anoxia-tolerant through the process of intracellular

305   denitrification (Schieber, 2011). Milliken et al., (2007) also note that modern

306   agglutinated foraminifera are highly tolerant to conditions of low oxygenation.

307   Furthermore, benthic foraminifera can colonize previously anoxic seafloor during short-

308   termed re-oxygenation events rather quickly whereas element geochemistry will still

309   record dominantly anoxic conditions, leading to the well known "anoxic benthic

14

310   foraminifera" paradox (Friedrich, 2010). We therefore propose that aerobic near-surface

311   sediment and bottom water conditions prevailed, but were temporally and spatially

312   restricted.

313   Assuming that the agglutinated foraminifera are *in situ*, rather than resuspended via

314   bottom currents, their occurrence suggests that the surface sediments were soft and that

315   strong surface water flow or scouring was absent (Kaminski & Schroder, 1987). This

316   would argue for a pelagic rather than turbidite or contourite depositional setting. To

317   emphasize, such an interpretation may well have been inferred from the apparent copious

318   occurrence of silt and sand particles. Given that it has been shown that different

319   agglutinated foraminifera morphotypes are found associated with a particular water

320   depth, infaunal niche, and oxygen levels (Kaminski et al.*,* 1995), further studies may well

321   prove interesting, but are beyond the scope of this manuscript.

322   The spherical to lenticular porosity, which is a common feature of the Colombian shale

323   (Z39), has a number of possible interpretations. In the case of the lenticular shaped

324   pores, these likely represent the locations of agglutinated benthic foraminifera that have

325   been plucked from the shale during sample preparation. More spherical pores may

326   instead represent sections through other agglutinated foraminifera, such as illustrated

327   herein (Fig. 5c, d), that have suffered a similar fate. They may alternatively represent

328   calcareous pelagic foraminifera (see Vergara et al, 1997), where the test has suffered

329   dissolution during diagenesis, or silicified algal cells (*Tazmanites*), such as those

330   illustrated from Devonian black shales by Schieber (1996), which have also been lost

331   during sample preparation. A number of these pores show an association between carbon

332   and sulphur, so may represent the remnants of *Tazmanites* (silicified or otherwise) or

15

333 possibly 'organic' filled remnants of dissolved pelagic foraminifera. *Tazmanites* has

334 been clearly observed in other Colombian black shales (*pers. obs.*). If, as seems likely, a

335 proportion of the pores represent plucked-out benthic agglutinated foraminifera, this

336 would be of particular interest, as it supports the widespread distribution of such

337 foraminifera, and thus rapid fluctuations in seafloor oxygenation levels through time.

338

339   **Implications**

340 Charge contrast imaging (CCI) enables differentiation of detrital and authigenic quartz

341 components within the silt-size fraction of mudrocks, comparable to applications on

342 carbonates and arenites. In particular, the characteristic mottled appearance of authigenic

343 micro-quartz clearly separates it from detrital silt-sized particles of quartz. Without

344 complementary data from CCI, the quartz sand component of a shale can easily be

345 overestimated if only apparent detrital grain size and elevated relative Si contents are

346 considered. This has profound implications for the interpretation of hydrodynamics of

347 the environment of deposition; possibly representing lower-energy conditions than would

348 otherwise have been interpreted from apparent high-levels of quartz silt. We show that

349 CCI unambiguously identifies the presence of agglutinated foraminifera, which provide

350 additional information on the depositional environment that might otherwise be

351 overlooked, such as degree of sediment / water interface oxygenation levels, sediment

352 consistency, and hydrodynamics. In addition, CCI provides information of a similar

353 character to that usually supplied by CL, although with an improvement in resolution and

354 speed of acquisition. The high levels of silicification recorded from the Zipa and La

355 Cristalina sections represent relatively early micro-quartz formation, with silica sourced

16

356 from siliceous micro-organisms, forming pervasive micrometer sized granular masses.

357 This contrasts with wavy micro-quartz noted from the Algodones area, formed from the

358 smectite-illite transformation at greater depth within the basin.

359

360   **Acknowledgements**

367

368   **References**

369   Al-Bazali, T.M., Zhang, J., Chenevert, M.E., and Sharma, M.M. (2005) Measurement of

370   the sealing capacity of shale caprocks. SPE Annual Technical Conference and

371   Exhibition, Dallas, Texas, USA, 9-12 October 2005.

372   Anjum, F., Shahid, M., and Akcil, A. (2012) Biohydrometallurgy techniques of low grade

373   ores: a review on black shales. Hydrometallurgy, 117-118, 1-12

374   Arango, C., and Hay, W.W. (1999) Plate tectonic paleoceanographic hypothesis for

375   Cretaceous source rocks and cherts of northern South America. Evolution of the

376   Cretaceous ocean-climate, 191.

377   Bennett, R.H., Bryant, W.R., and Hulbert, M.H. (1991) Microstructure of Fine-grained

378   Sediments, from Mud to Shale, 582 p. Springer-Verlag, New York.

379   Bjørlykke, K., and Egeberg, P.K. (1993) Quartz cementation in sedimentary basins.

380   AAPG Bulletin, 77, 1538-1548.

381   Buckman, J.O., Corbett, P.W.M., and Mitchell, L. (2016) Charge contrast imaging

382   (CCI): revealing enhanced diagenetic features of a coquina limestone. Journal of

383   Sedimentary Research, 86, 734-748.

384   Blatt, H. (1970) Determination of mean sediment thickness in the crust: a sedimentologic

385   method. Geological Society of America Bulletin, 81, 255-262.

386   Brumsack, H.J. (2006) The trace metal content of recent organic carbon-rich sediments:

387   implications for Cretaceous black shale formation. Palaeogeography, Palaeoclimatology,

388   Palaeoecology, 232, 344–361

389   Camp, W.K., Diaz, E., and Wawak, B. (2013) Electron microscopy of shale

390   hydrocarbon reservoirs, memoir 102. The American Association of Petroleum

391   Geologists, Tulsa, 260 p.

392   Cuthbert, S.J., and Buckman, J.O. (2005) Charge contrast imaging of fine-scale

393   microstructure and compositional variation in garnet using the environmental scanning

394   electron microscope. American Mineralogist, 90, 701-707.

395   Doehne, E., and Carson, D. (2001) Charge contrast imaging (CCI) in the environmental

396   scanning electron microscope: optimizing operating parametres for calcite. Microscopy

397   and Microanalysis, 7, 780-781.

398   Elliott, W.C., and Matisoff, G. (1996) Evaluation of kinetic models for the smectite to

399   illite transformation. Clays and Clay Minerals, 44, 77-87.

400   Erlich, R.N., Villamil, T., and Keens-Dumas, J. (2003) Controls on the deposition of

401   Upper Cretaceous organic carbon-rich rocks from Costa Rica to Suriname. In C.

402   Bartolini, R.T. Buffler, and J. Blickwede, eds., The Circum-Gulf of Mexico and the

403   Caribbean: Hydrocarbon habitats, basin formation, and plate tectonics: AAPG Memoir

404   79, 1-45.

405   Friedrich, O. (2010) Benthic foraminifera and their role to decipher paleoenvironment

406   during mid-Cretaceous Oceanic Anoxic Events – the "anoxic benthic foraminifera"

407   paradox. Revue de Micropaleontologie, 53, 175-192.

408   Galvis-Portilla, H.A., Higuera-Diaz, I., Cespedes, S., Ballesteros, C., Forero, S., Marfisi,

409   N., Cantisano, M, Pineda, E., Pachon, Z., Slatt, R.M., Ramirez, R., Guzman, G., and

410   Torres, A. (2014) Regional sequence stratigraphy of the Upper Cretaceous La Luna

19

411   Formation in the Magdalena Valley Basin, Colombia. Unconventional Resources

412   Technology Conference, Denver, Colorado, USA, 25-27 August 2014.

413   Garcia-Gonzalez, M. (2010) Shale gas potential in the Eastern Cordillera of

414   Colombia. AAPG Bulletin, 10286.

415   Ghiara, M.R., and Petti, C. (1995) Chemical alteration of volcanic glasses and related

416   control by secondary minerals: Experimental studies. Aquatic Geochemistry, 1, 329-354.

417   Gómez Tapias, J., and Almanza Meléndez, M.F. (ed) (2015) Compilando la Geología de

418   Colombia: Una visión a 2015. Servicio, Geológico Colombiano, Publicaciones

419   Geológicas Especiales 33.

420   Griffin, B.J. (1997) A new mechanism for the imaging of crystal structure in non-

421   conductive materials: an application of charge-induced contrast in the environmental

422   scanning electron microscope (ESEM). Microscopy and Microanalysis, 3, 1197-1198.

423   Griffin, B.J. (2000) Charge contrast imaging of material growth and defects in ESEM:

424   linking electron emission and cathodoluminescence. Scanning, 22, 234.

425   Guerrero, J. (2002) A proposal on the classification of systems tracts: Application to the

426   allostratigraphy and sequence stratigraphy of the Cretaceous Colombian Basin. Part 2:

427   Barremian to Maastrichtian. Geología Colombiana, 27, 27-49.

428   Hurst, A. (1985) Diagenetic chlorite formation in some Mesozoic shales from the

429   Sleipner area of the North Sea. Clay Minerals, 20, 69-79.

20

430   Ibbeken, H., and Schleyer, R. (1991) Source and Sediment: A Case Study of Provenance

431   and Mass Balance at an Active Plate Margin (Calabria, Southern Italy), 286 pp. Springer-

432   Verlag, New York.

433   Kaminski, M.A., and Schroder, C.J. (1987) Environmental analysis of deep-sea

434   agglutinated foraminifera: can we distinguish tranquil from disturbed environments?

435   Gulf Coast Section SEPM Foundation Proceedings of the 8th Annual Research

436   Conference, 90-93.

437   Kaminski, M.A., Boersma, A., Tyszka, J., and Holbourn, A.E.L. (1995) Response of

438   deep-water agglutinated foraminifera to dysoxic conditions in the California Borderlands

439   basins. In Kaminski, M.A., Geroch, S., and Gasinski, M.A. (eds), Proceedings of the

440   Fourth International Worksop on Agglutinated Foraminifera, Kraków Poland, September

441   12-19, 1993, pp. 131-140. Grzybowski Foundation Special Publication no 3.

442   Lazar, O.R., Bohacs, K.M., Macquaker, J.H.S., Schieber, J., and Demko, T.M. (2015)

443   Capturing key attributes of fine-grained sedimentary rocks in outcrops, cores, and thin

444   sections: nomenclature and description guidelines. Journal of Sedimentary Research, 85,

445   230-246.

446   Lehmann, K., Berger, A., Götte, T., and Wiedenbeck, M. (2009) Growth related

447   zonations in authigenic and hydrothermal quartz characterized by SIMS, EPMA, SEM-

448   CL- and SEM – CC-imaging. Mineralogical Magazine, 73, 633-643.

21

449   Macellari, C.E., and DeVries, T.J. (1987) Late Cretaceous upwelling and anoxic

450   sedimentation in northwestern South America. Palaeogeography, Palaeoclimatology,

451   Palaeoecology, 59, 279-292.

452   Mello, J.F. (1971) Foraminifera from the Pierre Shale (Upper Cretaceous) at Red Bird,

453   Wyoming. Geological Survey Professional Paper 393-C, United States Government

454   Printing Office, Washington, 53 p., 7 plates.

455   Milliken, K.L., Choh, S.-J., Papazis, P., and Schieber, J. (2007) "Cherty" stringers in the

456   Barnett Shale are agglutinated foraminifera. Sedimentary Geology, 198, 221-232.

457   Milliken, K.L. (2013) SEM-based cathodoluminescence imaging for discriminating

458   quartz types in mudrocks. Unconventional Resources Technology Conference, Denver,

459   Colorado, USA. URTeC 1582467.

460   Milliken, K. (2014) A compositional classification for grain assemblages in fine-grained

461   sediments and sedimentary rocks. Journal of Sedimentary Research, 84, 1185-1199.

462   Milliken, K.L., Ergene, S.M., and Ozkan, A. (2016) Quartz types, authigenic and

463   detrital, in the Upper Cretaceous Eagle Ford Formation, South Texas, USA. Sedimentary

464   Geology, 339, 273-288.

465   Mora, A., Casallas, W., Ketcham, R.A., Gomez, D., Parra, M., Namson, J., and Ghorbal,

466   B. (2015) Kinematic restoration of contractional basement structures using

467   thermokinematic models: a key tool for petroleum system modelling. AAPG Bulletin,

468   99, 1575-1598.

22

469   Olabode, A., Bentley, L., and Radonjic, M. (2012) Shale caprock integrity under carbon

470   sequestration conditions. Porous Media and its Applications in Science, Engineering, and

471   Industry. American Institute of Physics Conference Proceedings, 1453, 347-352.

472   Parra, M., Mora, A., Sobel, E.R., Strecker, M.R., and González, R. (2009) Episodic

473   orogenic front migration in the northern Andes: Constraints from low-temperature

474   thermochronology in the Eastern Cordillera, Colombia. Tectonics, 28, TC4004,

475   doi:10.1029/2008TC002423.

476   Perez-Infante, J., Farrimond, P., and Furrer, M. (1996) Global and local controls

477   influencing the deposition of the La Luna Formation (Cenomanian – Campanian),

478   western Venezuela. Chemical Geology, 130, 271-288.

479   Rani, N., Shrivastava, J.P., Bajpai, RKJ. (2012) Near hydrothermal alteration of

480   obsidian glass: Implications for long term performance assessments. Journal of the

481   Geological Society of India, 79, 376-382.

482   Schieber, J. (1996) Early diagenetic silica deposition in algal cysts and spores: a source of

483   sand in black shales? Journal of Sedimentary Research, 66, 175-183.

484   Schieber, J. (2009) Discovery of agglutinated benthic foraminifera in Devonian black

485   shales and their relevance for the redox state of ancient seas. Paleogeography,

486   Paleoclimatology, Paleoecology, 271, 292-300.

487   Schieber, J. (2011) Styles of agglutination in benthic foraminifera from modern Santa

488   Barbara Basin sediments and the implications of finding fossil analogs in Devonian and

489   Mississippian black shales, p 573-590. In Altenbach, A.V., Bernard, J.M., and Seckbach,

23

490   J. (eds.), Anoxia: evidence of eukaryote survival and paleontological strategies. Springer

491   Science and business media, 648 p.

492   Thyberg, B., Jahren, J., Winje, T., Bjørlykke, K., Faleide, J.I., and Marcussen, Ø. (2010)

493   Quartz cementation in Late Cretaceous mudstones, northern North Sea: Changes in rock

494   properties due to dissolution of smectite and precipitation of micro-quartz crystals.

495   Marine and Petroleum Geology, 27, 1752-1764.

496   Tribovillard, N.P., Stephan, J.F., Manivit, H., Reyre, Y., Cotillon, P., and Jautée, E.

497   (1991) Cretaceous black shales of Venezuelan Andes: preliminary results on stratigraphy

498   and paleoenvironmental interpretations. Palaeogeography, Palaeoclimatology,

499   Palaeoecology, 81, 313-321.

500   Vergara, L.S. (1997) Stratigraphy, foraminiferal assemblages and paleoenvironments in

501   the Late Cretaceous of the Upper Magdalena Valley, Colombia (Part I). Journal of South

502   American Earth Sciences, 10, 111-132.

503   Vergara, L., Rodríguez, G., and Martínez, I. (1997) Agglutinated foraminifera and

504   sequence stratigraphy from the Chipaque Formation (Upper Cretaceous) of El Crucero

505   Section, Colombia, South America. Micropaleontology, 43, 185-201.

506   Villamil, T., & Arango, C. (1994) High-resolution analyses of the Cenomanian-Turonian

507   Boundary in Colombia: evidence for sea level rise, condensation and upwelling.

508   Mesozoic-Cenozoic stratigraphy and tectonic evolution of the Caribbean Region /

509   Northern South America: Implications for eustasy from exposed sections of a Cretaceous-

510   Eocene passive margin setting. - SEPM special publication

511   Villamil, T., Arango, C., and Hay, W.W. (1999) Plate tectonic paleoceanographic

512   hypothesis for Cretaceous source rocks and cherts of northern South America. In Barrera,

513   E., and Johnson, C.C. (eds), Evolution of the Cretaceous Ocean-Climate system, 191-202.

514   Geological Society of America, Special Paper 332.

515   Watt, G.R., Griffin, B.J., and Kinny, P.D. (2000) Charge contrast imaging of geological

516   materials in the environmental scanning electron microscope. American Mineralogist,

517   85, 1784-1794.

518   Wedepohl, K.H. (1971) Environmental influences on the chemical composition of

519   shales and clays. Physics and Chemistry of the Earth, 8, 305-333.

520

521

522   **Figure Captions**

523

524   **Figure 1. a**) Locality map, showing geological units, and locality of sample Z39 from

525   the Chipaque Formation. Locations of other samples illustrated in the current work also

526   given. Both location names and sample identifiers are given.   **b**) General location map,

527   with context of area in (**a**) shown in white box. MMV = Middle Magdelana Valley, EC =

528   Eastern Cordillera. After Gómez Tapias and Almanza Meléndez (2015).

529

530   **Figure 2.** Stratigraphic distribution of formations and major facies within the Middle

531   Magdelana Valley (MMV) Basin and Eastern Cordillera (EC). Approximate

532   geographical and stratigraphic position of all samples marked: (1) Z39, (2) LC224, (3)

533   PE119, (4) C29, (5) P145, (6) M320, (7) P1+100, (8) Q1+70, (9) A240. Generalised

534   stratigraphy based on Parra et al., (2009). C= Conaician, T= Turonian.

535

536   **Figure 3. a**) Backscattered (BSE) stitched image of the whole polished thin-section for

537   sample Z39, showing lamination. **b**) BSE image of area marked in (**a**), displaying detail

538   of lamination, lenticular (*L*) and spherical (*S*) porosity, and pore lining Fe oxides (*Fe*).

539   Large porosity may be an artifact of plucking during sample preparation. **c**) BSE image

540   of detrital quartz silt particles (*Dq*) and authigenic micro-quartz (*Mq*). **d**) and **e**) BSE

541   and charge contrast matched pair of micrographs, illustrating micro-quartz (*Mq*) in

542   association with clay (*Cy*). All images are of sample Z39.

543

544   **Figure 4.** SEM micrographs illustrating fabric of silicified shale (Z39). **a**) Backscattered

545   electron image (BSE), **b**) – **f**) gaseous secondary electron images (GSE), exhibiting

546   charge contrast (CC), illustrating a number of features. In (**a**), a large silt particle (*St*) is

547   surrounded by authigenic micro-quartz (*Mq*). Silt particle appears to be 15 µm long. In

548   (**b**), charge contrast imaging (CCI) demonstrates that the detrital quartz (*Dq*) silt grain

549   also comprises an authigenic 'syntaxial' quartz overgrowth (*Qo*), as well as authigenic

550   micro-quartz (*Mq*). Similar relationships are also shown in (**c**) to (**f**). In addition in (**c**),

551   healed fractures (*f*) are observed, testifying to periods of compaction and grain shattering

552   prior to cementation. Note polishing scratches (s) on slides may be highlighted by the

553   CCI technique.

554

555   **Figure 5.** Charge contrast SEM micrographs illustrating occurrence of siliceous biogenic

556   structures and nature of micro-quartz cement within sample Z39. **a**) – **b**) Agglutinated

557   foraminifera, longitudinal section, overview and expanded view. Key as in figure 4, with

558   addition of agglutinated foraminifera (*Af*). Note lenticular shape in **a**) and the individual

559   quartz silt particles in (**b**). **c**) – **d**) Agglutinated foraminifera, transverse section,

560   overview and expanded view. Note the occurrence of clay (*Cy*), and individual silt

561   particles with syntaxial overgrowths (*1-6*). **e**) Detail of mottled micro-quartz, each

562   around 1 µm or less in size. Note euhedral shape to some of the micro-quartz (*Eo*).

563

564   **Figure 6.** Comparison of **a**) backscattered, **b**) charge contrast image, **c**)

565   cathodoluminescence image, and **d**) energy dispersive x-ray (EDX) map; all images taken

566   of the same field of view from sample Z39. (**b**) Shows the boundary between detrital

27

567 core and overgrowth (arrows). Cathodoluminescence image in (**c**) displays poor contrast

568 and lack of detail, which is atypical of CL, despite the use of high kV (20kV), large spot

569 size and long dwell times. X-ray dot map in (**d**) indicates quartz (1), clays (2), and pores

570 (3).

571

572 **Figure 7.** Charge contrast SEM micrographs illustrating degree of authigenic siliceous

573 micro-quartz cement, through the stratigraphic succession, in comparison to Z39: **a**)

574 LC224 (La Cristalina), **b**) PE119 (Pescana), **c**) C29 (Crucero), **d**) P145 (Pedregal), **e**)

575 M364 (La Marina), **f**) P1+100 (Pedregal), **g**) Q1+70 (Quemado), **h**) A240 (Algodones).

576 **a**) – **h**) Increasing in stratigraphic depth (see Table 4). **a**), **b**) High silicification, with

577 plentiful quartz overgrowths on detrital quartz silt grains, and micro-quartz, **c**) low degree

578 of silicification, comprising small amount of authigenic micro-quartz, **d**) - **g**) no to

579 limited occurrence of micro-quartz (only small quartz silt particles), **h**) low degree of

580 silicification, with localized areas displaying micro-quartz with a wavy morphology.

581 Note **a**) from Middle Magdelana Valley (MMV) and **b**)-**h**) from Eastern Cordillera (EC).

582 **Figure 8.** XRD trace for sample Z39, showing prevalence of quartz (all unlabeled

583 peaks), with minor illite (indicated by d-spacing values). Note the lack of peaks

584 associated with smectite that would appear on the far left-hand side of the graph. Two

585 minor peaks occur on the left-hand side (denoted by ?), but have no clear identity.

586 Sample analysed through powder XRD using Cu target, of the whole sample, with no

587 treatment other than crushing to a fine powder. Analysis of Z39 (<2um fraction) with

588 glycolation confirms lack of illite-smectite, the presence of minor kaolinite and

589 dominance of illite (Table 1).

28

590

591   **Figure 9.** BSE SEM micrograph, illustrating the dissolution of biogenic silica (from a

592   sponge spicule) and replacement with pyrite, from the Fomeque Formation (sample

593   LC224, La Cristalina).

594

595   **Figure 10.** Palaeogeographical reconstruction, during the Upper Cretaceous, within the

596   study area. Based on Arango and Hay (1999). Illustrating the general distribution of

597   facies, and orientation of the depositional basin. Basin connected to open ocean to the

598   north-east. Areas illustrated that are rich in chert and or phosphatic–rich deposits indicate

599   high productivity rates. Small black arrows indicate location of "wind-driven" upwelling,

600   white arrows direction of shallow water flow, grey arrows river flow, and large black

601   arrow direction of trade winds, after Erlich et al., (2003) and Arango and Hay (1999).

602

603

604   **Table Captions**

605

606   **Table 1.** XRD data for the greater than 2 μm and less than 2 μm fractions from locations

607   within the current study. Samples from beds examined in thin-section during the study

608   are in ***bold italic***. Data gathered using a Siemens D500 XRD. Key: Carb = carbonate, I/S

609   = illite-smectite, I = illite, K = kaolinite, ND = none detected, TR = trace levels. Note no

610   data collected from La Cristalina (e.g. LC224) or La Marina (e.g. M364), which is

611   indicated by X. Locations arranged in approximate stratigraphic order.

612

613   **Table 2.** XRF data for Zn/Al, Cu/Al and Ni/Al. Sample # refers to the examined thin-

614   sections, while data within brackets is an average figure for the different recorded

615   locations. Number of samples is 18, 20, 50, 25, 17, 21, 17, 12 and 21 respectively.

616   Samples arranged in approximate stratigraphic order.

617

618   **Table 3.** Element enrichment factors (EEF) for Mo, V, U and Zn relative to average shale

619   (Wedepohl, 1971). Areas that are relatively enriched are shaded in light grey.

620

621   **Table 4.** Table of data for samples examined during the current study. With data on

622   location, formation, stage, description, degree of silicification, overburden, and

623   temperature. Overburden and temperature data from Mora et al., (2015). Note figures in

624   brackets for temperature refer to the degree of error. Samples arranged in approximate

625   stratigraphic order. MMV = Middle Magdelana Valley, EC = Eastern Cordillera, [*] with

626   kaolinite and detrital quartz filled burrows, [**] irregular wavy authigenic micro-quartz

627   with clay.

30

Table 1

Location	>2 µm						<2 µm				
	Clay	Sand	Feldspar	Carb	Pyrite	TiO$_2$	I/S	I	K	Micro-quartz	Chlorite
PESCANA	*23*	*60*	*7*	*ND*	*<5*	*TR*	*ND*	*27*	*59*	*14*	*ND*
	68	17	<5	ND	ND	<5	13	28	54	5	ND
	38	52	<5	ND	TR	TR	ND	63	32	5	ND
	10	85	TR	ND	TR	TR	ND	34	34	32	ND
	27	68	ND	ND	ND	TR	ND	23	58	19	ND
	8	77	<5	TR	<5	TR	ND	18	18	64	ND
ZIPA	14	81	TR	ND	ND	TR	ND	60	<5	35	ND
	<5	90	ND	ND	ND	ND	ND	42	<5	53	ND
	39	56	ND	ND	TR	TR	ND	90	5	5	ND
	10	*85*	*ND*	*ND*	*ND*	*TR*	*ND*	*82*	*<5*	*13*	*ND*
	25	70	ND	ND	TR	TR	ND	68	12	20	ND
	11	84	ND	ND	TR	TR	ND	73	<5	22	ND
LA CRISTALINA	X	X	X	X	X	X	X	X	X	X	X
CRUCERO	62	33	TR	ND	ND	TR	15	20	45	20	ND
	63	*27*	*TR*	*ND*	*TR*	*<5*	*22*	*13*	*59*	*6*	*ND*
	77	18	TR	ND	TR	TR	18	23	50	9	ND
	35	55	ND	ND	TR	<5	25	50	20	<5	ND
	77	18	TR	ND	TR	TR	43	25	32	ND	ND
	74	21	TR	ND	TR	TR	8	47	40	<5	ND
PEDREGAL	65	20	TR	ND	<5	<5	ND	63	37	ND	ND
	38	42	<5	ND	5	<5	5	65	25	<5	ND
	46	39	TR	<5	TR	<5	ND	45	49	6	ND
	25	65	ND	ND	ND	<5	ND	50	40	10	ND
	63	22	TR	ND	<5	<5	ND	65	35	ND	ND
	38	47	TR	ND	<5	<5	ND	66	34	ND	ND
LA MARINA	X	X	X	X	X	X	X	X	X	X	X
QUEMADO	46	44	TR	ND	5	ND	ND	82	4.5	5	8
	50	40	<5	ND	TR	ND	ND	94	ND	6	ND
	60	25	<5	ND	<5	ND	ND	70	9	9	12
	52	33	<5	ND	<5	ND	ND	80	<5	10	<5
	38	52	<5	ND	ND	ND	ND	100	ND	ND	ND
ALGODONES	57	33	<5	ND	ND	ND	ND	95	ND	<5	ND
	50	40	<5	ND	TR	ND	ND	95	ND	<5	ND
	65	*20*	*<5*	*ND*	*<5*	*ND*	*ND*	*90*	*<5*	*<5*	*ND*
	86	9	TR	ND	ND	ND	ND	59	25	ND	16
	55	40	TR	ND	ND	ND	ND	76	15	ND	9
	67	23	<5	ND	ND	ND	ND	95	ND	<5	ND

Table 1. XRD data for the greater than 2 µm and less than 2 µm fractions from locations

within the current study. Samples from beds examined in thin-section during the study are in

bold italic. Data gathered using a Siemens D500 XRD. Key: Carb = carbonate, I/S = illite-

smectite, I = illite, K = kaolinite, ND = none detected, TR = trace levels. Note no data

collected from La Cristalina (e.g. LC224) or La Marina (e.g. M364), which is indicated by X.

Locations arranged in approximate stratigraphic order.

Table 2

Sample #	Location	Zn/Al	Cu/Al	Ni/Al
PE119	Pescana	6.94 (10.85)	0.71 (0.41)	1.65 (2.18)
Z39	Zipa	27.25 (66.65)	8.81 (7.32)	9.02 (16.88)
LC224	La Cristalina	67.53 (254.92)	4.49 (11.75)	22.27 (37.86)
C29	Crucero	1.69 (4.97)	0.52 (0.44)	1.03 (1.57)
P145	Pedregal	2.75 (4.93)	1.01 (1.17)	3.21 (2.87)
M364	La Marina	4.51 (5.59)	0.36 (0.51)	0.93 (1.99)
P1+100	Pedregal	1.48 (4.93)	0.74 (1.17)	1.27 (2.87)
Q1+70	Quemado	1.42 (1.95)	2.84 (1.6)	4.15 (2.89)
A240	Algodones	4.18 (4.38)	1.58 (1.61)	3.07 (2.52)

Table 2. XRF data for Zn/Al, Cu/Al and Ni/Al. Sample # refers to the examined thin-sections, while data within brackets is an average figure for the different recorded locations. Number of samples is 18, 20, 50, 25, 17, 21, 17, 12 and 21 respectively. Samples arranged in approximate stratigraphic order.

Table 3.

Location	Mo EEF	V EEF	U EEF	Zn EEF
Pescana	0.77	0.79	1.86	0.99
Zipa	11.63	7.32	8.59	6.06
La Cristalina	139.90	29.66	9.73	23.17
Crucero	1.28	0.71	1.44	0.45
Pedregal	0.23	0.68	2.24	0.45
La Marina	16.71	1.75	1.35	0.51
Quemado	17.17	1.25	1.23	0.18
Algodones	9.24	1.11	1.12	0.39

Table 3. Element enrichment factors (EEF) for Mo, V, U and Zn relative to average

shale (Wedepohl, 1971). Areas that are relatively enriched are shaded in light grey.

Table 4

Sample #	Location	Formation	Stage	Description	Silicification	Overburden (m)	Temp (˚C)
Z39	MMV, Zipa	Chipaque	Coniacian	Shale, some silt	High	3500-4000	78 (±9), 115 (±17)
LC224	MMV, La Cristalina	Fomeque	Cenomanian	Shale, some silt	Moderate-High	4800	162 (±25)
PE119	EC, Pescana	Chipaque	Campanian	Silty-fine sandstone	High	3500-4000	78 (±9), 115 (±17)
C29	EC, Crucero	Chipaque	Cenomanian	Shale, some silt	Low	3500-4000	78 (±9), 115 (±17)
P145	EC, Pedregal	Fomeque	Barremian	Silty shale	None	7000	208 (±20), 237 (±20)
M364	EC, La Marina	Fomeque	Hauterivian	Shale, some silt	None	7000	208 (±20), 237 (±20)
P1+100	EC, Pedregal	Fomeque	Hauterivian	Shale, silty layers*	None	7000	208 (±20), 237 (±20)
Q1+70	EC, Quemado	Macanal	Valangian	Silty shale	None	8500	249 (±8)
A240	EC, Algodones	Macanal	Valangian	Micaeous siltstone	Low**	8500	249 (±8)

Table 4. Table of data for samples examined during the current study. With data on location, formation, stage, description, degree of silicification, overburden, and temperature. Overburden and

temperature data from Mora et al., (2015). Note figures in brackets for temperature refer to the degree of error. Samples arranged in approximate stratigraphic order. MMV = Middle Magdelana Valley,

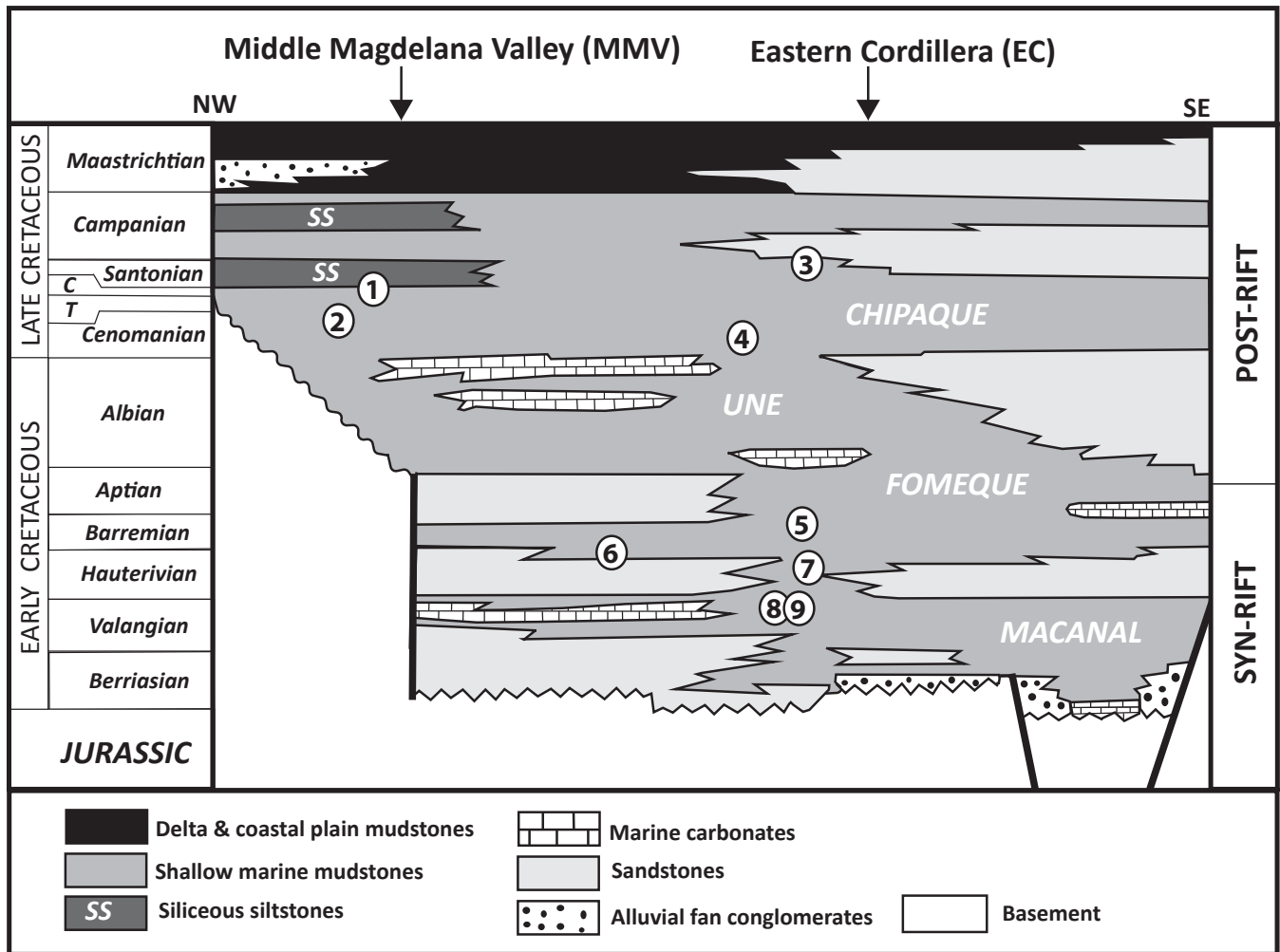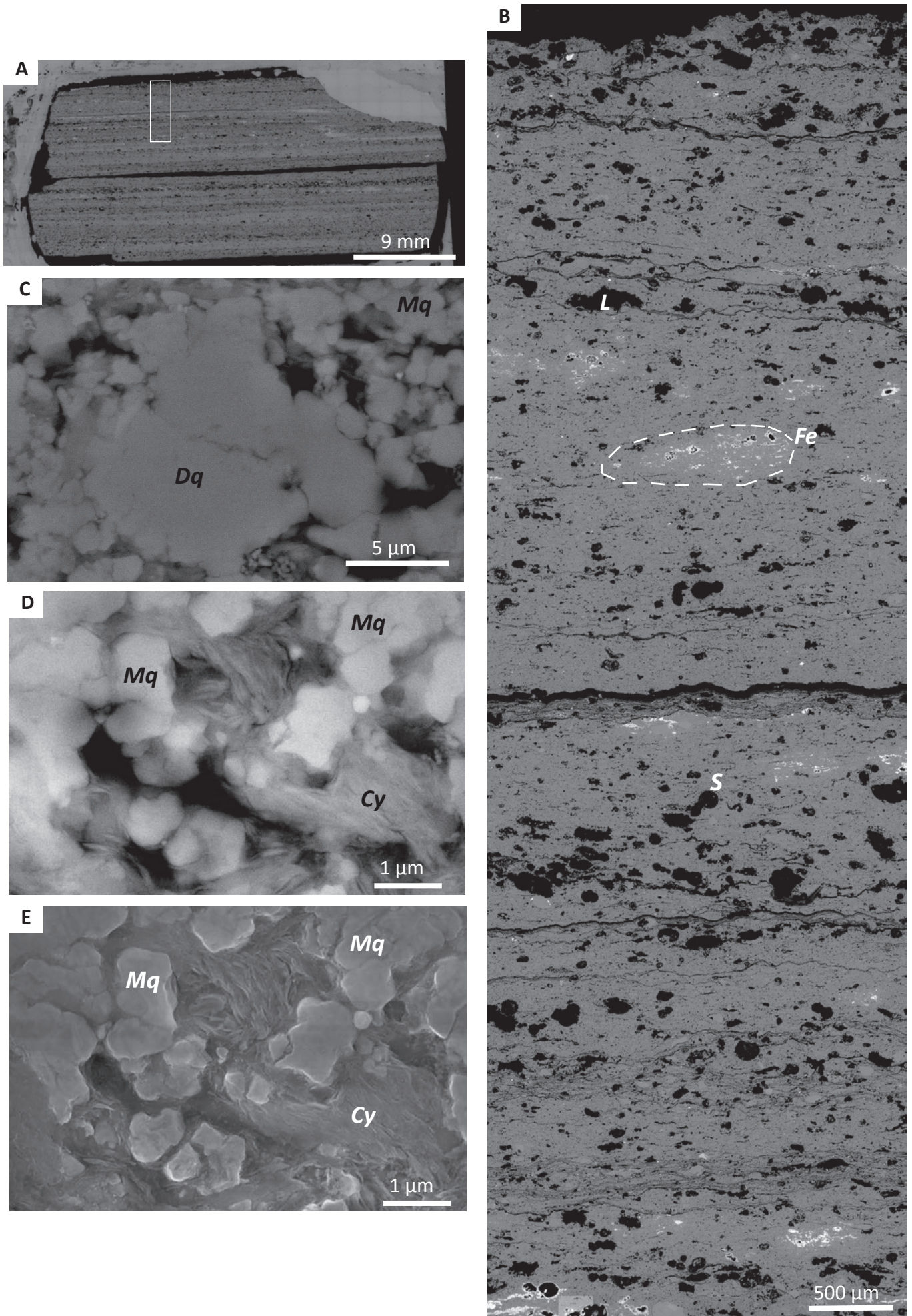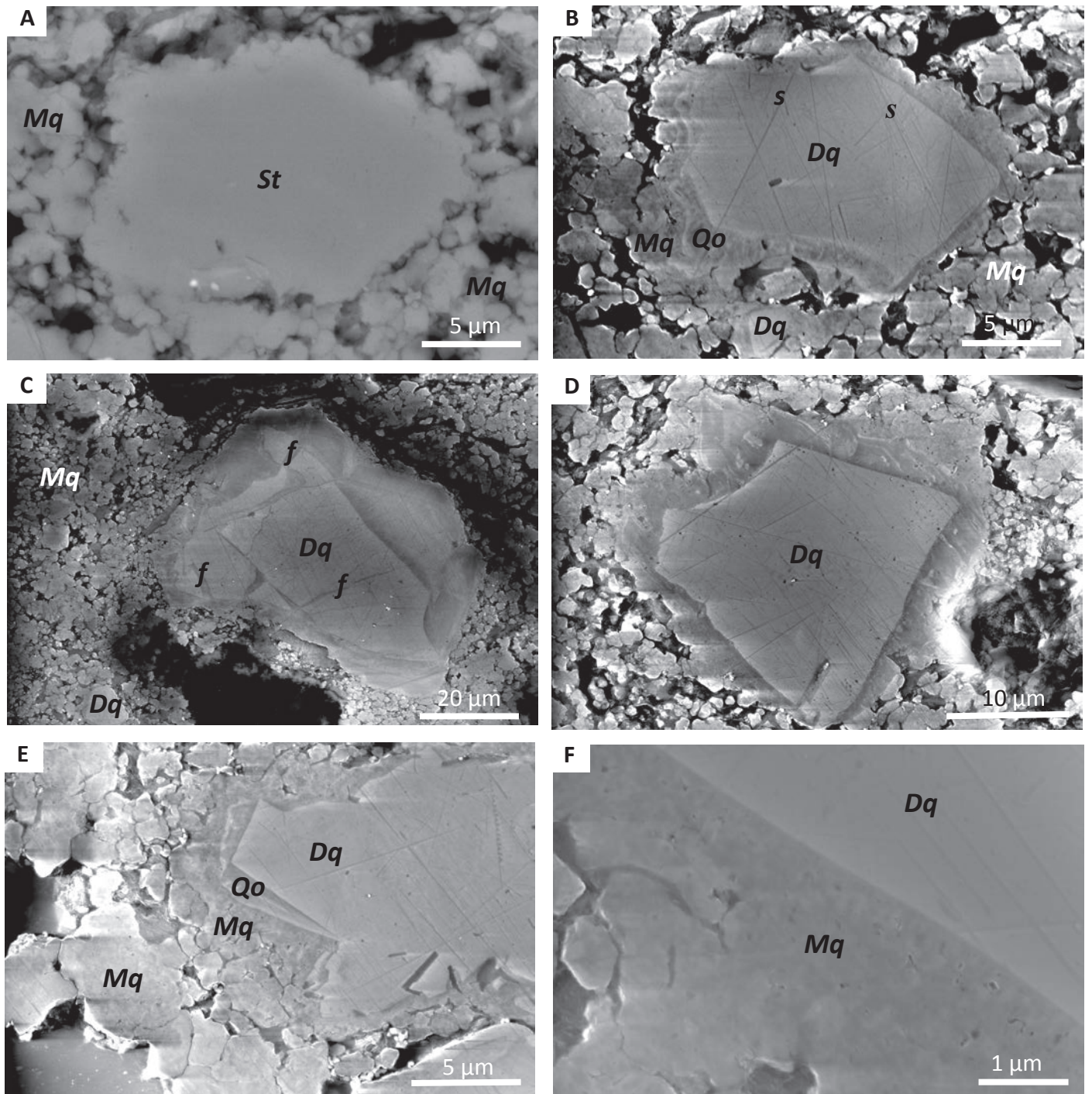EC = Eastern Cordillera, * with kaolinite and detrital quartz filled burrows, ** irregular wavy authigenic micro-quartz with clay.
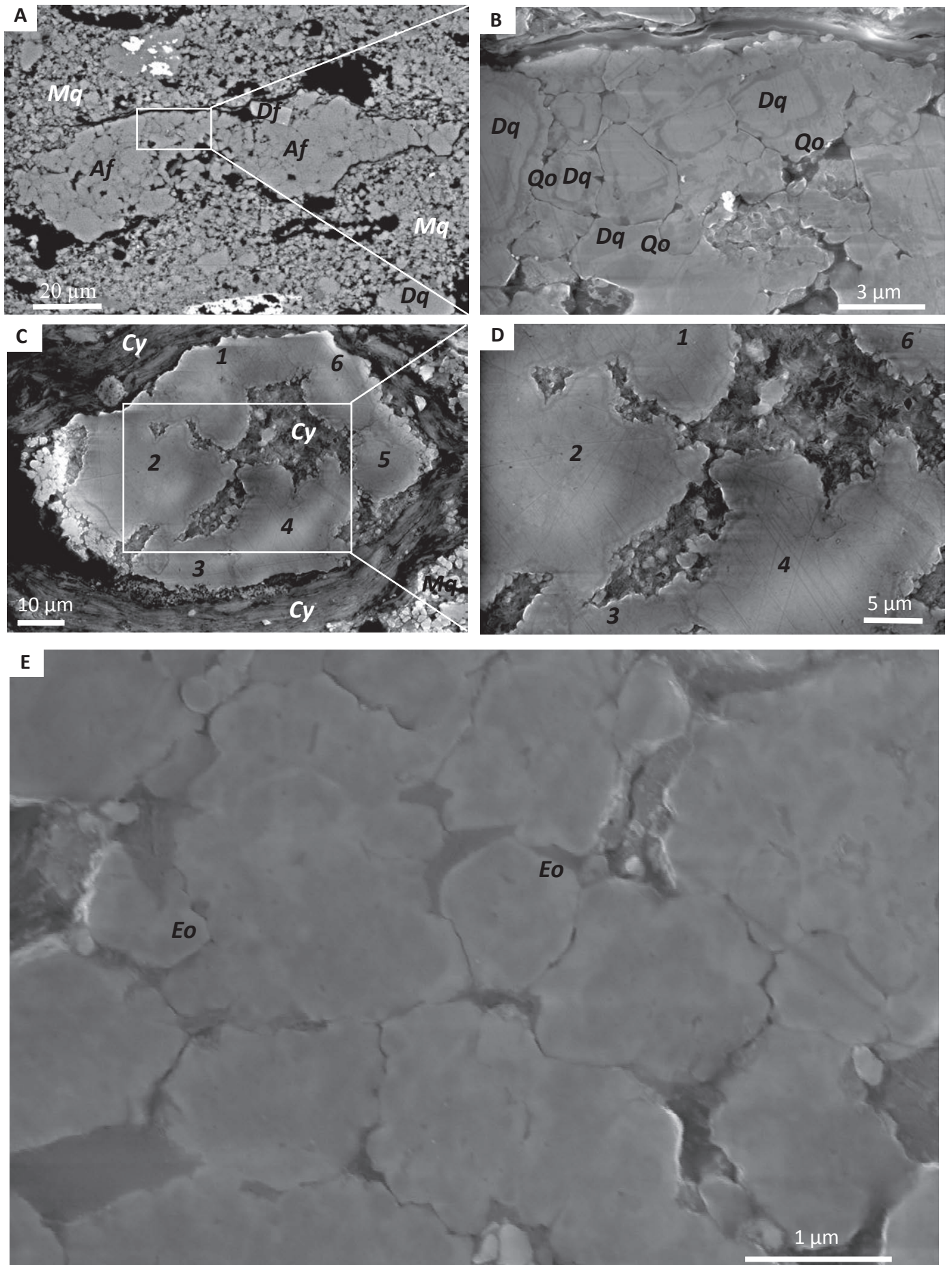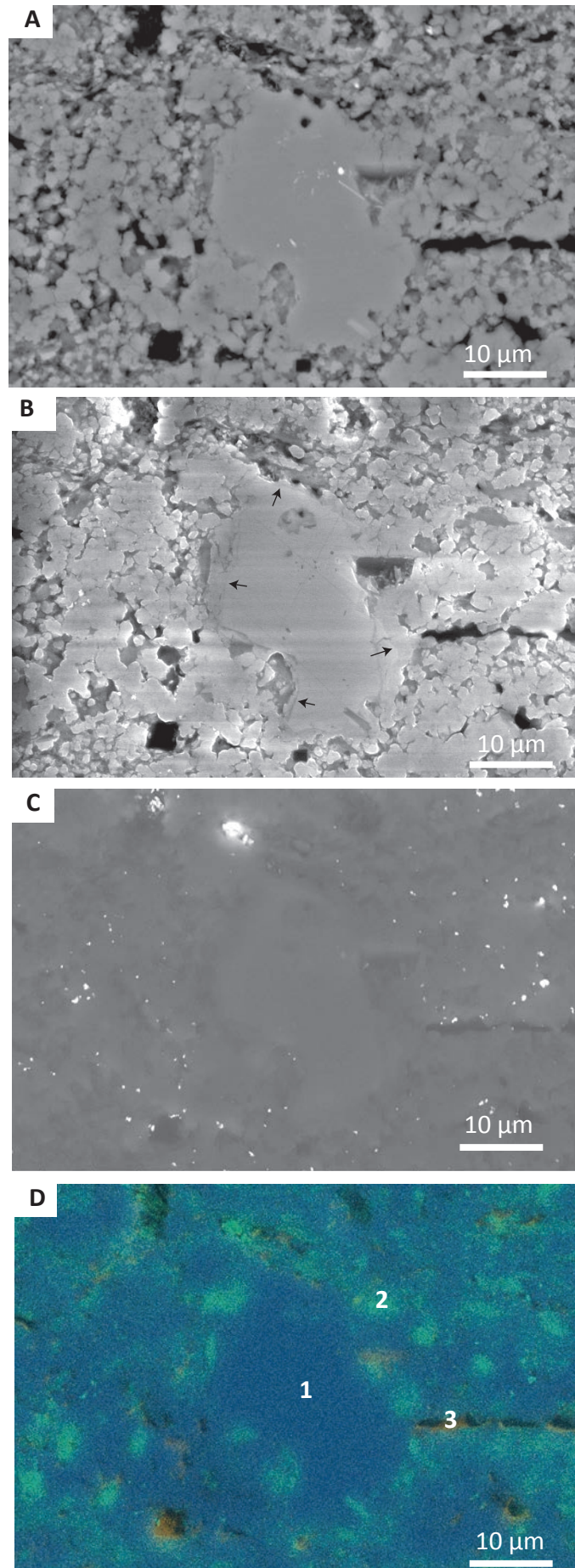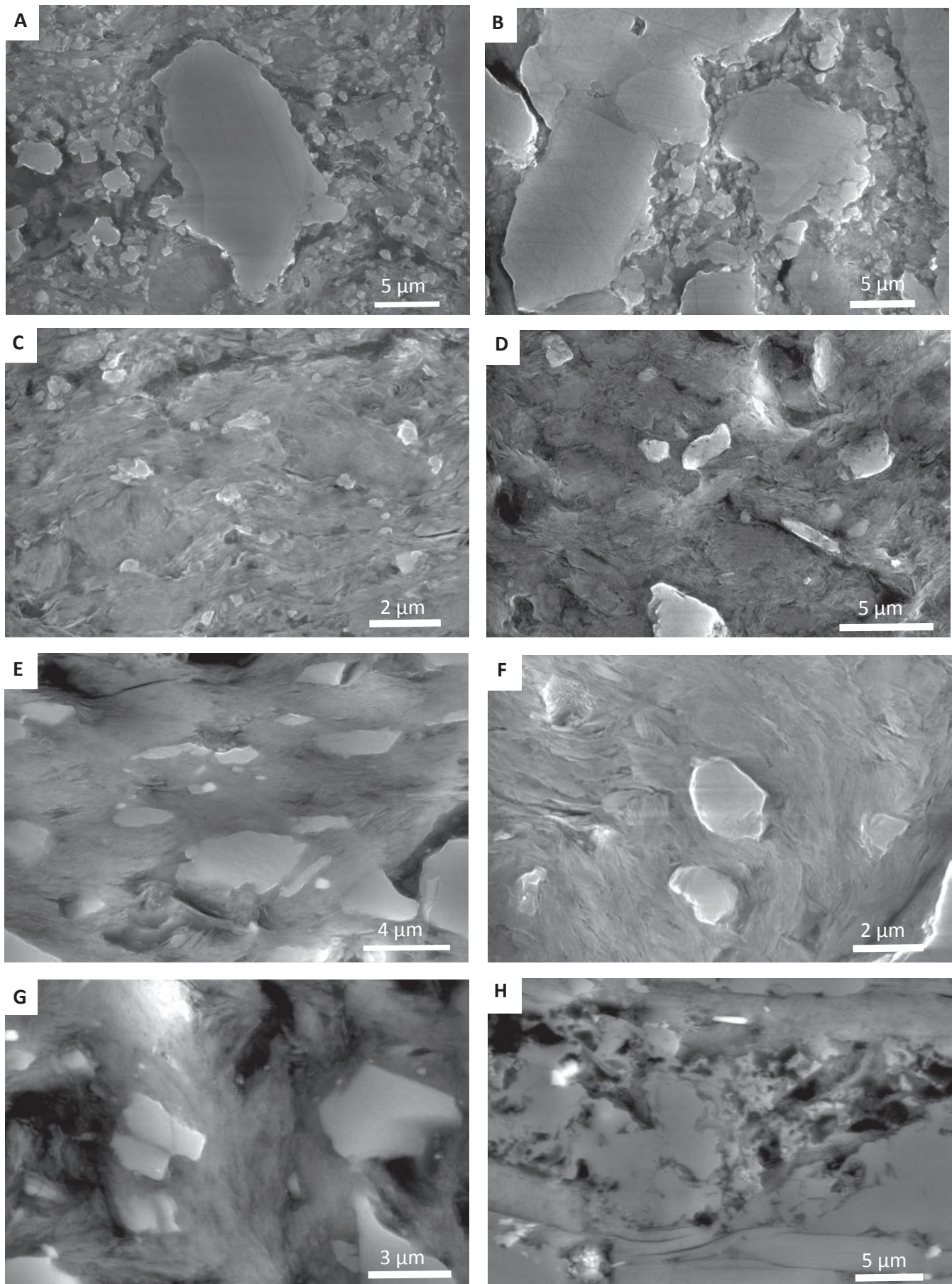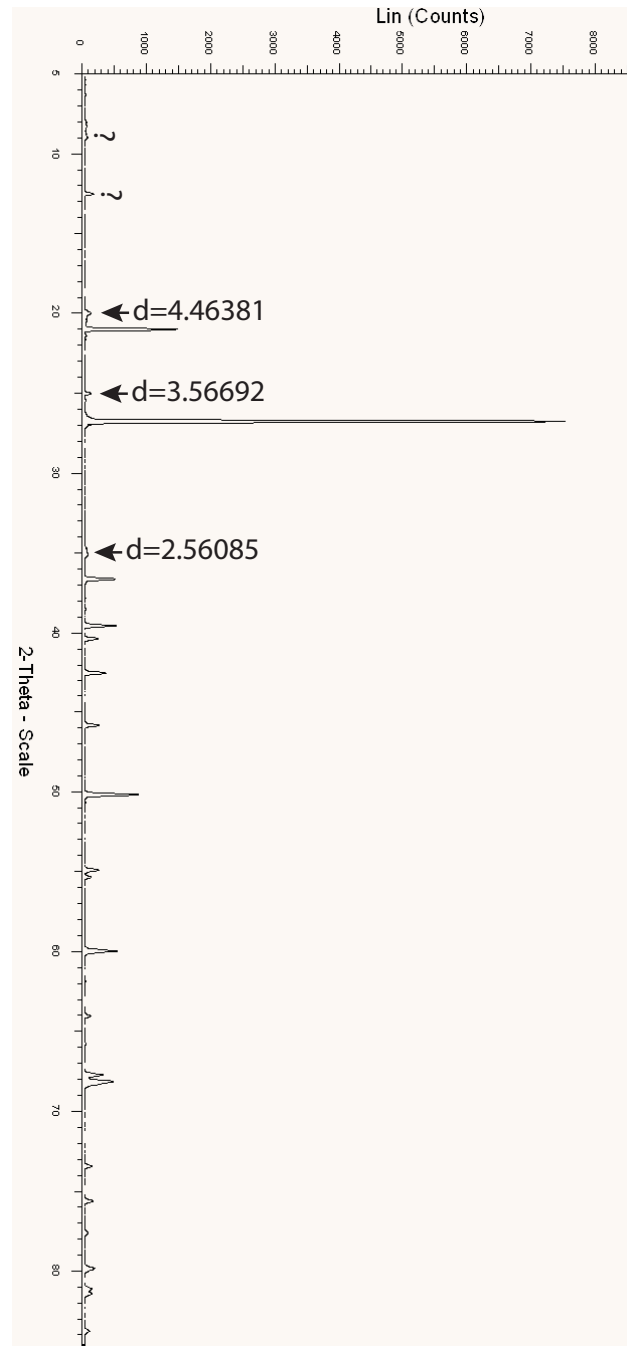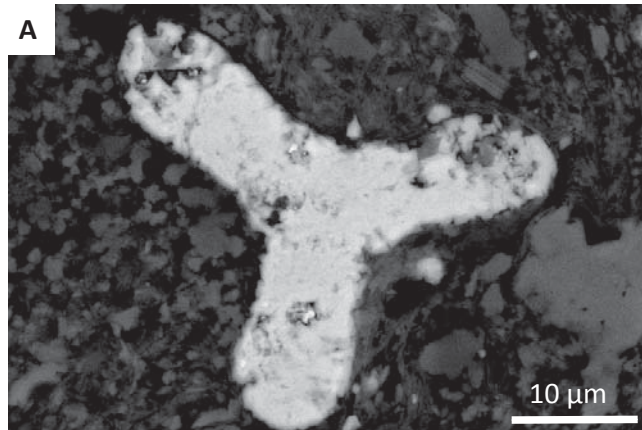
Figure 1
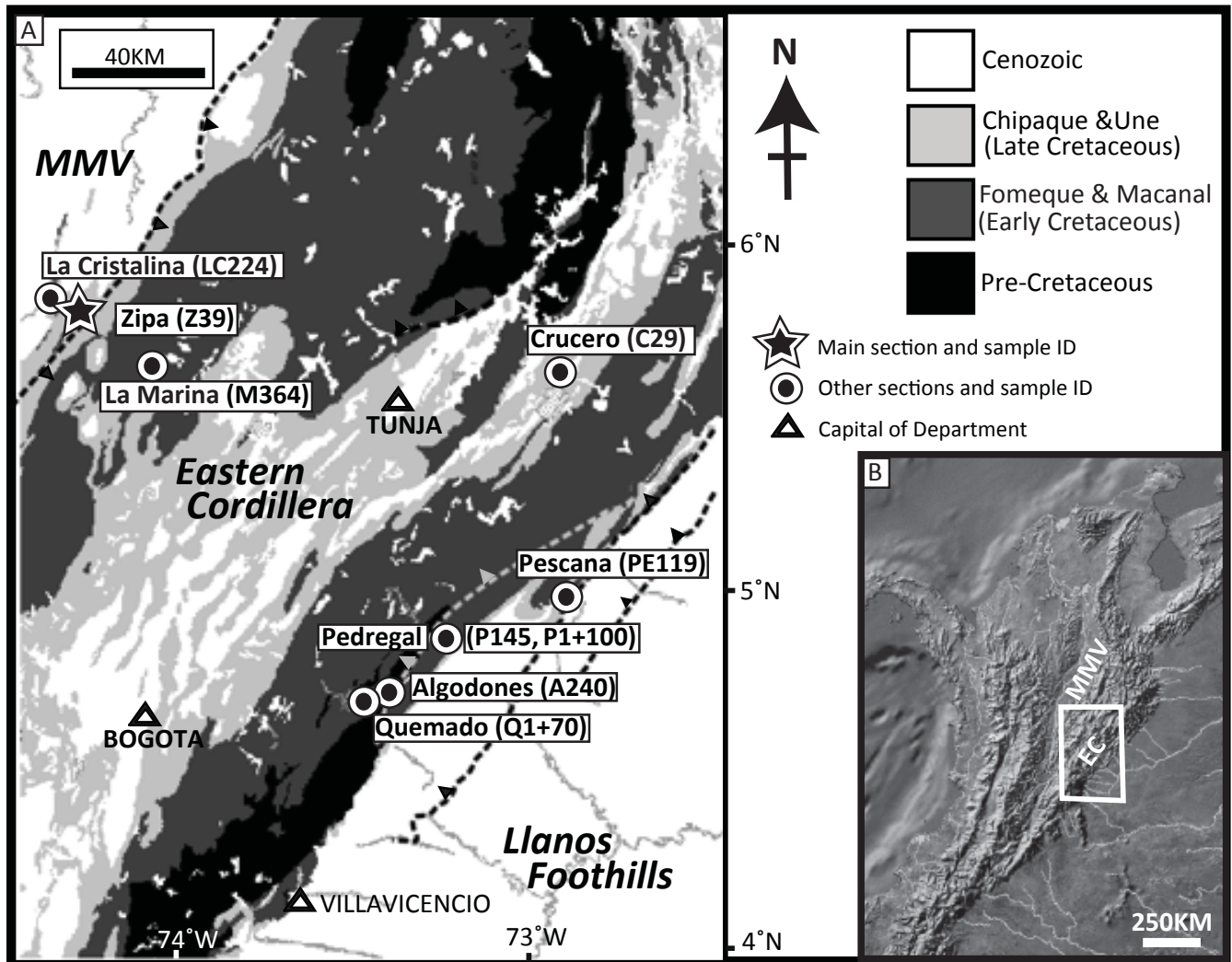
Figure 2

Figure 3

Figure 4

Figure 5

Figure 6

Figure 7

Figure 8

Figure 9

Figure 10